Positional Dependence of SNPP VIIRS Solar Diffuser BRDF Change Factor: An Empirical Approach

Ning Lei*, Xiaoxiong Xiong, Qiaozhen Mu, Sherry Li, and Tiejun Chang

***Abstract*—The Earth-observing Visible Infrared Imaging Radiometer Suite (VIIRS) on the Suomi National Polar-orbiting Partnership satellite regularly performs on-orbit radiometric calibration of its reflective solar bands (RSBs), primarily through observations of an onboard sunlit solar diffuser (SD). The on-orbit change of the SD bidirectional reflectance distribution function (BRDF) value, quantified by a numerical factor called the H-factor, is determined by the onboard SD stability monitor. Our previous study showed that the H-factor is solar angle and view direction dependent. In this study, we determine the dependence of the H-factor on the detector SD view footprint location. We fit an empirical model to the NASA Collection 1 SNPP VIIRS Level 1B (L1B) spectral reflectance difference across the detectors in an RSB over uniform Earth scenes of the Libya 4 desert and deep convective clouds. We apply the model predicted SD positional dependent H-factor to calibrate the RSBs. Under this new calibration scheme, the original unreal striping is removed from the homogeneous Libya 4 desert and the deep convective cloud images, as well as the original unreal striping from the Dunhuang desert image. The SD positional dependent H-factor has been used to calculate the SNPP VIIRS RSB radiometric correction factor for the NASA Collection 2.0 SNPP VIIRS L1B products.**

Index Terms: SNPP VIIRS, radiometric calibration, reflective solar band, solar diffuser, BRDF change, positional dependence, striping

I. Introduction

The Visible Infrared Imaging Radiometer Suite (VIIRS) is a passive Earth-observing cross-track scanning satellite sensor with a wide swath (~3000 km), collecting data to generate more than 20 biogeophysical parameters for Earth studies [1-3]. The sensor telescope is the first optical component and rotates at a constant speed to scan the Earth and the onboard calibrators. The first VIIRS instrument is aboard the Suomi National Polar-orbiting Partnership (SNPP) satellite launched on October 28, 2011. The SNPP satellite has a mean altitude of 839 km and is maintained in a near Sun-synchronous orbit with an equator-crossing local time of 13:30 [4], [5]. The VIIRS continues the data collection missions of the Moderate Resolution Imaging Spectroradiometers (MODISs) on Terra and Aqua satellites [6], [7]. Among the 22 VIIRS spectral bands, 14 are designed to detect the Earth reflected sunlight, referred to as the reflective solar bands (RSBs), with band center wavelengths from 0.41 to 2.25 μm [8]. Among the RSBs, 11 are referred to as the moderate resolution bands (M-bands) and three are referred to as the imaging bands (I-bands), with nadir spatial resolutions of 750 m and 375 m, respectively. Each M-band consists of a linear array of 16 detectors and each I-band consists of 32 detectors arranged in a zig-zag linear form. Six of the 11 RSB M-bands are dual-gain bands, able to function over a large range of scene spectral radiance levels because these dual-gain bands can automatically change the detector electronic gain stage depending on the scene signal strength.

Regular on-orbit radiometric calibrations of the RSBs are performed to ensure data quality. VIIRS uses an onboard solar diffuser (SD) panel to diffusely scatter sunlight to provide a known spectral radiance for the calibration [8-12]. As illustrated in Fig. 1, sunlight passes through the holes in a plate called the SD screen and then strikes the SD surface. The SD panel is made from Space-Grade Spectralon from Labsphere, Inc. [9]. Light can penetrate deep into the polymers of the Spectralon and is scattered multiple times along the path so that the SD appears quite Lambertian [13]. The spectral radiance of the SD scattered sunlight is proportional to the product of the SD screen transmittance and the SD bidirectional reflectance distribution function (BRDF) value at the observation direction.

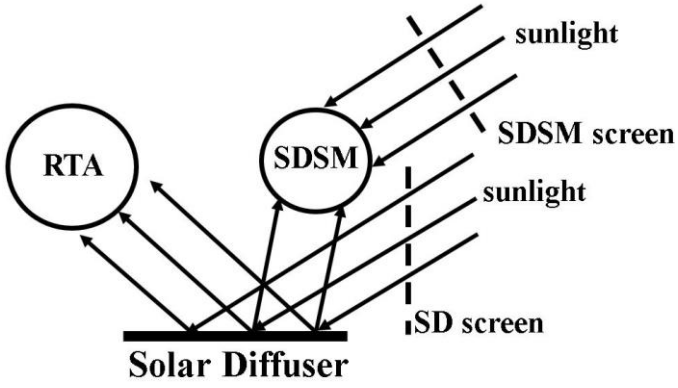


Fig. 1. A schematic showing the physical components related to the on-orbit RSB radiometric calibration of the SNPP VIIRS. The RTA is the rotating telescope assembly which directs incident light to the detector focal planes.

While the SNPP satellite is on orbit, the change in the SD BRDF value is determined by an onboard SD stability monitor (SDSM) [8], [9]. Overall, the SD BRDF value decreases over

* Ning Lei is with the Science Systems and Applications, Inc., Lanham, MD 20706 USA (e-mail: ning.lei@ssaihq.com).

Xiaoxiong Xiong is with Sciences and Exploration Directorate, NASA Goddard Space Flight Center, Greenbelt, MD 20771 USA (e-mail: xiaoxiong.xiong-1@nasa.gov).

Qizhen Mu is with the Science Systems and Applications, Inc., Lanham, MD 20706 USA (e-mail: qiaozhen.mu@ssaihq.com).

Sherry Li is with the Science Systems and Applications, Inc., Lanham, MD 20706 USA (e-mail: xuexia.chen@ssaihq.com).

Tiejun Chang is with the Science Systems and Applications, Inc., Lanham, MD 20706 USA (e-mail: tiejun.chang@ssaihq.com).

time, probably due to the SD's exposure to the Sun and other high energy particles in the space environment, combined with possible contaminants accumulated on orbit on the SD surface [14], [15]. Upon exposure to solar UV light, the contaminants can become yellow and absorb light, and scattering centers may also form (The scattering centers may be isolated and/or may comprise the collapsed top layers of the Spectralon polymers.). A numerical factor, called the H-factor [8], quantifies the on-orbit BRDF value change. We use H_{RTA} to denote the SD BRDF change factor along the telescope SD view direction.

The H-factor is angle dependent: on both the incident and outgoing directions [16], [17]. Additionally, the H-factor likely depends on the SD view footprint location, because the amount of solar energy received by a unit area of the SD surface likely depends on the area location, combined with possible non-uniform distributions of possible SD surface contaminants and scattering centers [18]. Across the detectors in a band and across the bands, the detector SD view footprints do not exactly overlap. The SD positional dependence of H_{RTA}, if not applied in the radiometric calibration, leads to unreal striping on Earth images.

In this paper, we develop an empirical model (Section III) to account for the dependence of H_{RTA} on the detector index in a band—the detector index in a particular band is used to indicate the location of the detector SD view footprint. Using the NASA Collection 1 (Archive Set 5000) SNPP VIIRS Level 1B (L1B) products over uniform scenes, we find the measured top-of-the-atmosphere (TOA) spectral reflectance differences among the detectors in a band and use these differences to determine the model parameter values. We apply the model to calculate the detector index dependent H_{RTA} to calibrate the RSBs for the L1B product Collection 2.0.

II. CALCULATION OF TOA SPECTRAL REFLECTANCE

To quantify the role of H_{RTA} in, and hence the impact of the detector SD view footprint position dependence of H_{RTA} on the retrieved TOA spectral reflectance, we briefly review the basic algorithms for the on-order SNPP VIIRS RSB radiometric calibration through observations of a sunlit SD.

For the VIIRS instrument, the TOA Earth scene spectral reflectance detected by detector *d* at time *t* is calculated by

$$\rho_{\mathrm{EV}}(t,d) = \frac{4\pi^2 F * P(dn_{\mathrm{EV}}) d^2_{\mathrm{VIIRS-SUN}} \times \int_0^\infty \mathrm{RSR}(\lambda,t,d)d\lambda}{\mathrm{RVS}(\lambda_{\mathrm{B}},\theta_{\mathrm{EV}})\cos\theta_{\mathrm{EARTH-SUN}} \times \int_0^\infty \mathrm{RSR}(\lambda,t,d)\Phi_{\mathrm{SUN}}(\lambda,t)d\lambda}. \quad (1)$$

In (1), *F*, known as the F-factor [8], is a numerical correction factor to the spectral radiance calculated by the polynomial, $P(dn_{\mathrm{EV}})$, of the Earth view detector's background subtracted digital number, dn_{EV}. $d_{\mathrm{VIIRS-SUN}}$ is the distance between the VIIRS and the Sun. RSR is the relative spectral response function of the detector, approximated by the average over the detectors in a band, λ is the sunlight wavelength, RVS is the reflectivity of the half-angle-mirror (HAM) at the incident angle of θ_{EV} relative to its value when the telescope views the center of the Space View port, $\theta_{\mathrm{EARTH-SUN}}$ is the angle between the incident sunlight and the normal vector of the Earth surface area that is observed by the detector, and Φ_{SUN} is the solar spectral power. The RVS was originally in the wavelength integral in the denominator and time dependent. Because the VIIRS HAM's reflectivity does not change much from the prelaunch value—since the telescope prevents most of the solar bombardment from striking the HAM, the wavelength dependence of the RVS is insignificant. Hence we took the RVS term out of the integral with the wavelength parameter replaced by the band center wavelength which is denoted by λ_{B}. We also approximated the RVS curve to be time invariant and hence removed the time variable in the RVS input variable list, supported by observations over deep convective clouds (DCCs) and deserts [19], [20]. One of the "πs" in the numerator in (1) is a scale factor, in unit of 1/steradiance. The scale factor purposely lets the reflectance be one for a Lambertian surface. $P(dn_{\mathrm{EV}})$ is defined as

$$P(dn_{\mathrm{EV}}) = c_0 + c_1 dn_{\mathrm{EV}} + c_2 {dn_{\mathrm{EV}}}^2, \quad (2)$$

in unit of [$\mathrm{Wm^{-2}sr^{-1}\mu m^{-1}}$]. In (2), the c-coefficients are detector focal plane and electronics temperature dependent and are obtained through interpolating the prelaunch values. In this paper, c_0 is set to zero.

For the SNPP VIIRS, on-orbit radiometric calibration of the RSBs centers on calculating the F-factor. Through the observation of the fully sunlit SD, the F-factor is given by

$$F(t,d) = \frac{\mathrm{RVS}(\lambda_{\mathrm{B}},\theta_{\mathrm{SD}})}{P(dn_{\mathrm{SD}})} \times \frac{\int_0^\infty \mathrm{RSR}(\lambda,t,B)L_{\mathrm{SD}}(\lambda,t)d\lambda}{\int_0^\infty \mathrm{RSR}(\lambda,t,B)d\lambda}. \quad (3)$$

In (3), θ_{SD} is the sunlight incident angle for the HAM, L_{SD} is the spectral radiance provided by the SD, dn_{SD} is the detector background subtracted digital number when viewing the SD. Like the reason for (1), the RVS term was originally inside the wavelength integral, but was taken out of the integral. The detector RSR is approximated by the RSR averaged across the detectors in a band. Since the RVS is HAM side dependent, and *dn* (both SD and Earth views) depends on the HAM side and the gain stage of a dual-gain detector, the F-factor depends on the HAM side and on the gain stage for a dual-gain detector. To reduce the complexity of our notations, the mathematical symbols in this paper do not explicitly use HAM side and gain-stage variables.

The SD spectral radiance is given by

$$L_{\mathrm{SD}}(\lambda,t) = \frac{\Phi_{\mathrm{SUN}}(\lambda,t)}{4\pi d^2_{\mathrm{VIIRS-SUN}}} \times \tau_{\mathrm{SD}}\mathrm{BRDF}_{\mathrm{RTA}}(\lambda,0,\vec{\phi})H_{\mathrm{RTA}}(\lambda,t,\vec{\phi})\sin\phi_{\mathrm{V,SD}}, \quad (4)$$

where τ_{SD} is the SD screen transmittance, $\mathrm{BRDF}_{\mathrm{RTA}}(\lambda,0,\vec{\phi})$, in units of 1/steradians, is the SD's BRDF value at the satellite launch time (*t*=0)—assumed to take the value measured prelaunch—along the SD-to-telescope direction and at the incident solar angle of $\vec{\phi}$, and $\phi_{\mathrm{V,SD}}$ is the angle between the incident sunlight and the SD surface.

H_{RTA} at a fixed $\phi_{\mathrm{V,SD}}$ is calculated from [21]

$$H_{\mathrm{RTA}}(\lambda,t,\phi^{\mathrm{RTA}}_{\mathrm{H,SD}}) = H_{\mathrm{SDSM}}(\lambda,t) \times \frac{1+\alpha_{\mathrm{RTA}}(\lambda)*(1-H_{\mathrm{SDSM}}(\lambda,t))}{1+\alpha_{\mathrm{H}}(\lambda)*(1-H_{\mathrm{SDSM}}(\lambda,t))*(\phi^{\mathrm{RTA}}_{\mathrm{H,SD}}-\phi_{\mathrm{H0}})}, \quad (5)$$

where H_{SDSM} is the SDSM detector RSR deconvolved H-factor along the SD-to-SDSM direction at the $\phi_{\mathrm{V,SD}}$ in (4), $\phi_{\mathrm{H,SD}}^{\mathrm{RTA}}$ is the solar azimuth angle defined as the angle between the Sun-to-VIIRS and SD-to-telescope vectors projected onto the SD plane, ϕ_{H0} is a reference solar azimuth angle on the SD plane, set at 48.0°, and α_{RTA} and α_{H} are the model parameters. In calculating both the F- and H-factors, we set $\phi_{\mathrm{V,SD}}$ to 35.5°.

The SDSM views a fixed area of the SD. We retrieve H_{SDSM}, using the time series of the signal strength ratio of the SDSM SD and Sun views. Hence the retrieved H_{SDSM} and the H_{RTA} given by (5) are independent of the position on the SD surface. To address the H-factor SD positional dependence along the detectors in a band, we add a detector index dependent factor to the H_{RTA} given by (5), as detailed in the next section.

III. AN EMPIRICAL MODEL OF H_{RTA} SD POSITIONAL DEPENDENCE

H_{SDSM} reflects how much the SD is degraded by the solar exposure. Hence we base our model on a function of H_{SDSM} with the detector index as the variable to indicate the detector SD view footprint center position. Although the simplest function is linear in H_{SDSM}, we use the retrieved SNPP VIIRS TOA spectral reflectance over uniform scenes to guide the model development.

Earth scenes have been widely used to calibrate Earth observing remote sensors [22], [23]. The TOA reflectances are from the deep convective clouds (DCCs) in the intertropical convergence zone at and around nadir [24], [25], and from the Libya 4 desert [26]. The DCC and Libya 4 desert reflectances are averaged over a month and a year, respectively. At a particular telescope scan angle, the DCC and Libya 4 images are expected to be uniform across the detector index if the on-orbit calibration was correctly performed. But the retrieved reflectance (NASA Archive Set 5000, known as Collection 1) is dominated by a linear relation with the detector index difference, as shown in Fig. 2. In the figure, the detector index difference of one means detector index 2 minus detector index 1 or detector index 3 minus detector index 2, and so on. The lower indexed detectors register higher spectral reflectances, as shown in Fig. 2. Consequently, we propose our H_{RTA} model for an M-band as

$$H_{\mathrm{RTA}}\left(\lambda, t, \phi_{\mathrm{H,SD}}^{\mathrm{RTA}}, \vec{r}_d\right) = H_{\mathrm{RTA}}\left(H_{\mathrm{SDSM}}(\lambda,t), \phi_{\mathrm{H,SD}}^{\mathrm{RTA}}\right) \times \left[1 + c_{d,1}(d - d_{\mathrm{mid}}) + c_{d,2}(d - d_{\mathrm{mid}}) \times \left(1 - H_{\mathrm{SDSM}}(\lambda,t)\right)\right], \quad (6)$$

where $\vec{r}_d$ indicates the SD view center location on the SD surface for the RSB detector d, $c_{d,1}$ and $c_{d,2}$ are the time independent model parameters, and d_{mid} of a value of 7.5 is the middle of the 16 detector indexes—the detector index starts from zero. For the I-bands, we group together detectors 0 and 1 to form a new detector 0, group detectors 2 and 3 together to form a new detector 1, and so on, so that we can also use (6). $H_{\mathrm{RTA}}\left(H_{\mathrm{SDSM}}, \phi_{\mathrm{H,SD}}^{\mathrm{RTA}}\right)$ in (6) denotes the H_{RTA} calculated by (5), by assuming that the SDSM SD view footprint has the same center as the SD view footprint for the hypothetical detector of index 7.5. The parameter $c_{d,1}$ reflects the difference in BRDF(t=0) across the SD surface.

To find the model parameter values in (6), we use (1), (3), (4), (6), and the property that the wavelength integral in (3) is dominated by the in-band part. If the true H_{RTA} behaves as that modeled by (6), then $P(dn_{\mathrm{SD}})$ is approximately proportional to $1 + c_{d,1}(d - d_{\mathrm{mid}}) + c_{d,2}(d - d_{\mathrm{mid}}) \times (1 - H_{\mathrm{SDSM}})$. Hence if the detector index dependence of H_{RTA} is not applied in the calculation of L_{SD}, over a uniform Earth scene, the retrieved TOA spectral reflectance relative difference will behave as

$$\frac{\rho_{\mathrm{EV}}(t,d) - \langle \rho_{\mathrm{EV}}(t,d)\rangle_d}{\langle \rho_{\mathrm{EV}}(t,d)\rangle_d} = -c_{d,1}(d - d_{\mathrm{mid}}) - c_{d,2}(d - d_{\mathrm{mid}}) \times \left(1 - H_{\mathrm{SDSM}}(\lambda_{\mathrm{B}}, t)\right), \quad (7)$$

where $\langle \cdots \rangle_d$ indicates the average across the detectors in a band. Hence, the relative reflectance difference between detectors 0 and 15 is

$$\frac{\rho_{\mathrm{EV}}(t, d=0) - \rho_{\mathrm{EV}}(t, d=15)}{\langle \rho_{\mathrm{EV}}\rangle_d} = 15c_{d,1} + 15c_{d,2}\left(1 - H_{\mathrm{SDSM}}(\lambda_{\mathrm{B}}, t)\right). \quad (8)$$

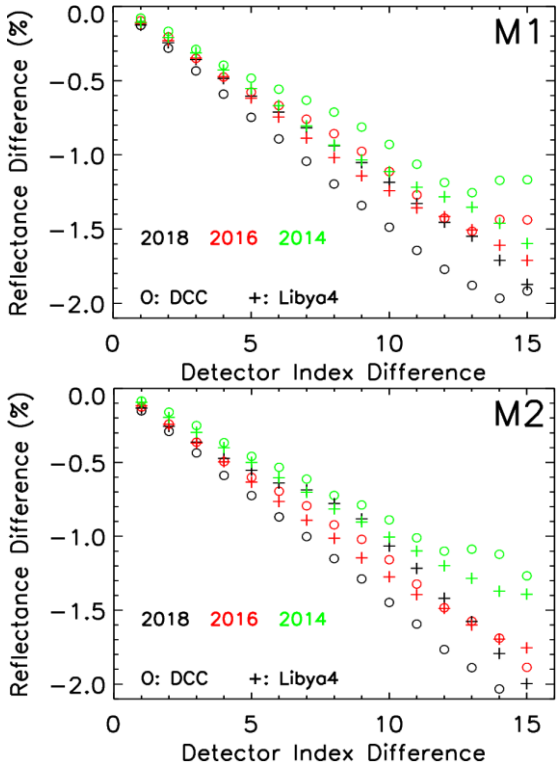


Fig. 2. Measured TOA spectral reflectance relative differences in percentage vs detector index difference for bands M1 (top) and M2 (bottom) over the DCCs (circles) and the Libya 4 desert (pluses) in 2014 (green), 2016 (red) and 2018 (black).

To find the TOA reflectance difference between detectors 0 and 15, we fit

$$\frac{\rho_{\mathrm{EV}}(t,d_2) - \rho_{\mathrm{EV}}(t,d_1)}{\langle \rho_{\mathrm{EV}}(t,d)\rangle_d} = c_d(t) \times (d_1 - d_2) \quad (9)$$

to the measured spectral reflectance differences for all detector

index differences, from $d_1 - d_2$ of 1 to 15. The measured spectral reflectance relative differences are from the DCCs and the Libya 4 site, as illustrated in Fig. 2, and the fit is performed separately for the DCC and the Libya 4 scenes. Due to saturation, measured reflectance results for the DCC and the Libya 4 scenes are not available for band M6. In performing the fit, we use a weight of 15 for the detector index difference of 1, 14 for the index difference of 2, and so on, to reflect that there are 15 pairs of the detector indexes with the index difference of 1, 14 pairs with the index difference of 2, and so forth.

We use the fit result of $c_d(t)$ for each band to find the spectral reflectance relative difference between detectors 0 and 15. Then we fit (8) to the spectral reflectance differences between detectors 0 and 15 to find $c_{d,1}$ and $c_{d,2}$, combining the measured results from both the DCC and the Libya 4 scenes with equal weights. Fig. 3 shows an example of the fits, for band M1.

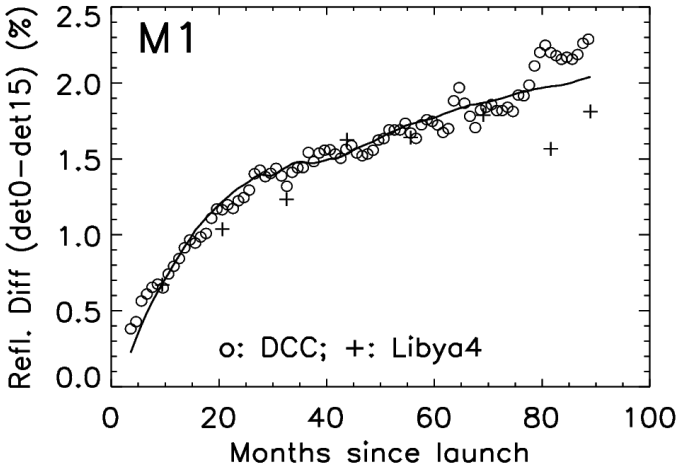


Fig. 3. Time series of the TOA spectral reflectance relative (to the mean reflectance of detectors 0 to 15) difference between detectors 0 and 15 over the DCCs (circles) and the Libya 4 desert (pluses), obtained by fitting (9) to the measured reflectance differences for band M1. The solid line is the least-squares fit of (8) to the circles and the pluses.

TABLE I
MODEL PARAMETER RESULTS

Band	$c_{d,1}10^4$	$c_{d,2}10^2$	std($c_{d,1}10^4$)	std($c_{d,2}10^2$)
I1	0.55	0.29	0.11	0.01
I2	1.17	0.77	0.09	0.04
M1	-0.96	0.33	0.24	0.01
M2	0.70	0.37	0.29	0.01
M3	2.94	0.19	0.17	0.01
M4	2.54	0.28	0.12	0.01
M5	0.00	0.00	0.12	0.02
M7	2.66	0.50	0.11	0.05

Our results show that the initial BRDF difference between detectors 0 and 15 has a magnitude smaller than 0.45%, with the largest difference magnitudes occurring for bands M3, M4, and M7. Bands M1 and M2 have the largest time dependence of the detector difference of H_{RTA}, with the difference magnitude between detectors 0 and 15 increasing from approximately zero at the mission start to slightly over 2.0% at 90-month in the mission. Table I lists the fitting results of $c_{d,1}$ and $c_{d,2}$ and their respective estimated standard deviations for the visible near infrared bands, except band M6. Band M6 detectors are located at one edge of the focal plane. Next to band M6 is band M5. For band M5, we do not see any H_{RTA} SD positional dependence. Hence, we set the H-factor SD positional dependence for band M6 to zero.

An alternative equivalent approach is to fit

$$\frac{\rho_{\mathrm{EV}}(t,d)}{\langle \rho_{\mathrm{EV}} \rangle_d} = \rho_0 + \mathrm{slope}(t)(d - d_{\mathrm{mid}}) \tag{10}$$

to the measured spectral reflectance values across the detectors for each (band, scene) and then fit $c'_{d,1} + c'_{d,2}\left(1 - H_{\mathrm{SDSM}}(\lambda_{\mathrm{B}}, t)\right)$ to the slopes—combining both scenes with equal weights. The magnitude of the slope reflects the strength of the detector index difference of H_{RTA}.

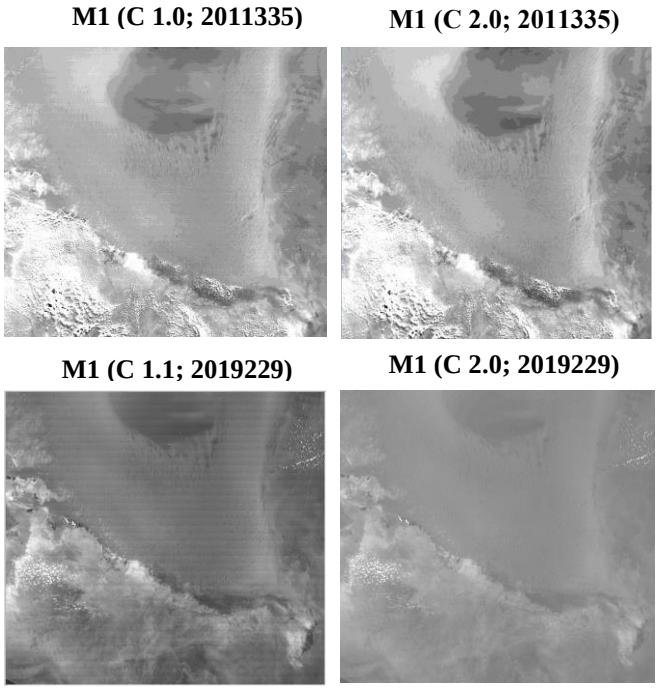


Fig. 4. Libya 4 images at an early mission time (335th day of 2011; top two images) and a recent time (229th day of 2019; bottom two images) taken by band M1. The left two images are for Collection 1, without the H-factor SD positional dependence; the right two images are calibrated with the H-factor SD positional dependence.

Using the fitting results of $c_{d,1}$ and $c_{d,2}$, we apply (6) to calculate $H_{\mathrm{RTA}}\left(\lambda, t, \phi_{\mathrm{H,SD}}^{\mathrm{RTA}}, \vec{r}_d\right)$ which is then used to calculate the F-factor (see (3)). We use the updated F-factors to generate the SNPP VIIRS RSB Look-Up-Tables (LUTs) and then we run the L1B code with the new LUTs to produce the TOA spectral reflectance to check whether the application of $H_{\mathrm{RTA}}\left(\lambda, t, \phi_{\mathrm{H,SD}}^{\mathrm{RTA}}, \vec{r}_d\right)$ removes the unreal striping in the Libya 4 desert images. As illustrated in Fig. 4 for band M1, the application of $H_{\mathrm{RTA}}\left(\lambda, t, \phi_{\mathrm{H,SD}}^{\mathrm{RTA}}, \vec{r}_d\right)$ successfully removes the original unreal striping in the Libya 4 images. The light striping, seen in the original M1 Libya 4 desert image (Archive Set 5000) at the early mission time of the 335th day in 2011 (top left), disappears (top right) after the detector index dependence is

applied. Similarly, the striping, of a magnitude of 1%, seen in the original M1 Libya 4 desert image at a recent time of the 229th day in 2019 (bottom left), disappears (bottom right) after the detector index dependence is applied. Another example to demonstrate the impact of the H-factor SD positional dependence is shown in Fig. 5. The figure shows the SNPP VIIRS band M1 L1B images of the Dunhuang desert which centers at the latitude of 40.18º and the longitude of 94.27º. The top image is calibrated with the F-factor LUTs without taking into account of the H-factor SD positional dependence whereas the bottom image is calibrated with the H-factor SD positional dependence as shown in (6). The striping in the top image is not present in the bottom image, as expected.

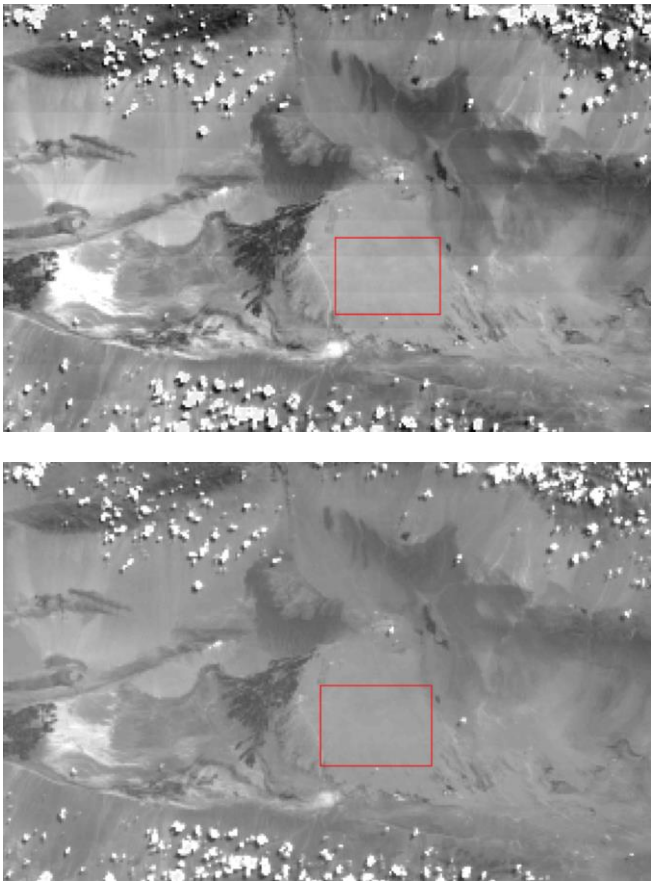


Fig. 5. SNPP VIIRS band M1 L1B images of the Dunhuang desert which centers at the latitude of 40.18º and the longitude of 94.27º (encircled by the red square) on August 8, 2020. The top image is for Collection 1, without the H-factor SD positional dependence and the bottom image is calibrated with the H-factor SD positional dependence.

Note that since the sunlight reflected by DCCs and deserts are polarized, the polarization sensitivity spread among the detectors in a band may lead to a detector index dependent DCC and desert TOA reflectance images as well. However, for the SNPP VIIRS, the detector polarization sensitivity spread's impact at the nadir view is very small. At the nadir view and the band M1 center wavelength, the reflected sunlight at TOA from a desert has a degree of polarization less than 0.05 at equinox [27] and less than 0.025 from thick clouds such as DCCs [28]. The polarization factors for the band M1 detectors at the nadir view are approximately 0.012 with a small spread of 0.002 [29]. The spread of the polarization phase angles among the band M1 detectors contributes a factor of approximately 0.5 to the reflectance spread. Hence, for band M1, the detector polarization sensitivity spread impacts on the DCC and the Libya 4 TOA reflectance spread by less than 0.033%, much smaller than what is shown in Fig. 3.

IV. SUMMARY

The primary means to calibrate on orbit the SNPP VIIRS reflective solar bands is to use an onboard sunlit solar diffuser. Due to solar exposure, combined with possible SD surface contaminants, the solar diffuser BRDF changes its value over time. The amount of the solar exposure and the surface density of the possible contaminants may not be the same across the SD surface. Hence the on-orbit SD BRDF value change may not be even across the SD surface. As a result, using a single on-orbit BRDF change factor, the H-factor, for all the detectors in an RSB for the radiometric calibration can yield inaccurate scene spectral radiance correction factors, the F-factors, and thus can lead to unreal striping in an Earth image, as shown in the NASA Collection 1 SNPP VIIRS Level 1B products at the Libya 4 and Dunhuang desert sites and over deep convective clouds. We have developed an empirical model of the H-factor that is a linear function of a detector's SD view footprint location to account for the L1B spectral reflectance differences across the detectors in an RSB, existed in the Collection 1 images of the Libya 4 desert and deep convective clouds. Applying the model to the H-factor, we have shown that the original striping in the Libya 4 and the Dunhuang L1B images has been removed. We have applied this model in the calculation of the H-factor for the NASA Collection 2.0 SNPP VIIRS Level 1B products.

ACKNOWLEDGMENT

We thank Kevin Twedt of the Science Systems and Applications, Inc., Lanham, MD USA for review comments.

REFERENCES

[1] C. Schueler, J. Clement, P. Ardanuy, C. Welsch, F. DeLuccia, and H. Swenson, "NPOESS VIIRS sensor design overview", in *Proc. SPIE*, Vol. 4483, pp. 11-23, 2012; doi: 10.1117/12.453451.

[2] R. P. Murphy, P. E. Ardanuy, F. De Luccia, J. E. Clement, and C. Schueler, "The visible infrared imaging radiometer suite", in *Earth Science Satellite Remote Sensing*, J. Qu, W. Gao, M. Kafatos, R. Murphy, V. Salomonson, Ed., Vol. 1, pp. 199-223, Springer-Verlag: New York, USA, 2006.

[3] R. E. Wolfe, G. Lin, M. Nishihama, K. Tewari, J. Tilton, and A. Isaacman, "Suomi NPP VIIRS prelaunch and on-orbit geometric calibration and characterization*", J. Geophy. Res.: Atmosphere*, Vol. 118, pp. 11508-11521, 2013; doi: 10.1002/jgrd.50873.

[4] C. Cao, F. J. De Luccia, X. Xiong, R. Wolfe, and F. Weng, "Early On-Orbit Performance of the Visible Infrared Imaging Radiometer Suite Onboard the Suomi National Polar-Orbiting

Partnership(S-NPP) Satellite", *IEEE Trans. Geosci. Remote Sens.*, Vol. 52, pp. 1142-1156, 2013; doi: 10.1109/TGRS.2013.2247768.

[5] G. Lin, R. Wolfe, J. Tilton, P. Zhang, J. Dellomo, and B. Tan, "JPPP-1/NOAA_20 VIIRS early on-orbit geometric performance", in *Proc. SPIE*, Vol. 10764, Art ID: 10764-1H, 2018; doi: 10.1117/12.2320767.

[6] X. Xiong, J. Sun, W. Barnes, W. Salononson, J. Esposito, H. Erives, and B. Guenther, "Multiyear On-Orbit Calibration and Performance of Terra MODIS Reflective Solar Bands", *IEEE Trans. Geosci. Remote Sens.*, Vol. 45, pp. 879-889, 2007; doi: 10.1109/TGRS.2006.890567.

[7] X. Xiong, J. Sun, X. Xie, W. Barnes, and V. Salomonson, "On-Orbit Calibration and Performance of Aqua MODIS Reflective Solar Bands", *IEEE Trans. Geosci. Remote Sens.*, Vol. 48, pp. 535-546, 2010; doi: 10.1109/TGRS.2009.2024307.

[8] Joint Polar Satellite System (JPSS) VIIRS Radiometric Calibration Algorithm Theoretical Basis Document (ATBD); NASA Goddard Space Flight Center: Greenbelt, MD, USA, 2013.

[9] J. Fulbright, N. Lei, B. Efremova, and X. Xiong, "Suomi-NPP VIIRS Solar Diffuser Stability Monitor Performance", *IEEE Trans. Geosci. Remote Sens.*, Vol. 54, pp. 631-639, 2016; doi: 10.1109/TGRS.2015.2441558.

[10] N. Lei, Z. Wang, and X. Xiong, "On-orbit Radiometric Calibration of Suomi NPP VIIRS Reflective Solar Bands through Observations of a Sunlit Solar Diffuser Panel", *IEEE Trans. Geosci. Remote Sens.*, Vol. 53, pp. 5983-5990, 2015; doi: 10.1109/TGRS.2015.2430814.

[11] R. Eplee, K. Turpie, G. Meister, F. Patt, B. Franz, and S. Bailey, "On-orbit calibration of the Suomi National Polar-Orbiting Partnership Visible Infrared Imaging Radiometer Suite for ocean color applications", *Applied Optics*, Vol. 54, pp. 1984-2006, 2015; doi: 10.1364/AO.54.001984.

[12] J. Sun and M. Wang, "Visible Infrared Imaging Radiometer Suite solar diffuser calibration and its challenges using a solar diffuser stability monitor", *Applied Optics*, Vol. 53, pp. 8571-8584, 2014; doi: 10.1364/AO.53.008571.

[13] C. Bruegge, A. Stiegman, R. Rainen, and A. Springsteen, "Use of Spectralon as a diffuse reflectance standard for in-flight calibration of earth-orbiting sensors", *Opt. Engineering*, Vol. 32, pp 805-814, 1993; doi: 10.1117/12.132373.

[14] A. E. Stiegman, D. E. Brinza, E. G. Laue, M. S. Anderson, and R. H. Liang, "Vacuum Ultraviolet Radiation/Atomic Oxygen Synergism in Fluorinated Ethylene Propylene Teflon Erosion", *J. Spacecraft and Rockets*, Vol. 29, pp. 150-151, 1992.

[15] A. E. Stiegman, C. Bruegge, and A. W. Springsteen, "Ultraviolet stability and contamination analysis of Spectralon diffuse reflectance material", *Opt. Engineering*, Vol. 32, pp. 799-804, 1993.

[16] N. Lei, K. Chiang, and X. Xiong, "Examination of the angular dependence of the SNPP VIIRS solar diffuser BRDF degradation factor", in *Proc. SPIE*, Vol. 9218, 2014, Art ID. 9218-1N.

[17] N. Lei and X. Xiong, "Products of the SNPP VIIRS SD Screen Transmittance and the SD BRDFs From Both Yaw Maneuver and Regular On-Orbit Data", *IEEE Trans. Geosci. Remote Sens.*, Vol. 55, pp. 1975-1987, 2017; doi: 10.1109/TGRS.2016.2633967.

[18] N. Lei, X. Chen, T. Chang, and X. Xiong, "Positional dependence of the SNPP VIIRS SD BRDF degradation factor", in *Proc. SPIE*, Vol. 10423, Nov. 2017, Art ID: 1042317; doi: 10.1117/12.2277715.

[19] Q. Mu, X. Xiong, T. Chang, and A. Wu, "Exploring the stability and residual response versus scan angle effects in SNPP VIIRS sensor data record reflectance products using deep convective clouds", *J. of Appl. Remote Sens.*, Vol. 12, 2018; doi: 10.1117/1.JRS.12.034006.

[20] A. Wu, X. Xing, and C. Cao, "Assessment of stability of the response versus scan angle for the S-NPP VIIRS reflective solar bands using pseudo-invariant desert and Dome C sites", in *Proc. SPIE*, Vol. 10423, 2017, Art ID: 10423-22; doi: 10.1117/12.2278380.

[21] N. Lei and X. Xiong, "Impact of the Angular Dependence of the Solar Diffuser BRDF Degradation Factor on the SNPP VIIRS Reflective Solar Band On-Orbit Radiometric Calibration", *IEEE Trans. Geosci. Remote Sens.*, vol. 55, pp. 1537-1543, 2017; doi: 10.1109/TGRS.2016.2626963.

[22] G. Chander, T. Hewison, N. Fox, X. Wu, X. Xiong, and W. J. Blackwell, "Overview of Intercalibration of Satellite Instruments", *IEEE Trans Geosci. Remote Sens.*, Vol. 51, issue 3, pp. 1056-1080, 2013.

[23] D. R. Doelling et al., "The characterization of deep convective clouds as an invariant calibration target and as a visible calibration technique," *IEEE Trans. Geosci. Remote Sens.*, Vol. 51, Issue 3, pp. 1147–1159, 2013.

[24] Q. Mu, X. Xiong, A. Wu, and A. Angal, "Assessment of SNPP VIIRS RSB detector-to-detector differences using deep convective clouds and deserts", *J. of Appl. Remote Sens.*, Vol. 14, 2020; doi: 10.1117/1.JRS.14.018503.

[25] T. Chang, X. Xiong, and Q. Mu, "VIIRS Reflective Solar Band Radiometric and Stability Evaluation Using Deep Convective Clouds", *IEEE Trans. Geosci. Remote Sens.*, Vol. 54, Issue 12, pp. 7009–7017, 2016

[26] X. Chen, N. Lei, and X. Xiong, "Suomi NPP VIIRS DNB and RSB M bands detector-to-detector and HAM side calibration differences assessment using a homogenous ground target", in *Proc. SPIE*, Vol. 10764, Sep. 2018, Art ID. 10785-0X; doi: 10.1117/12.2322153.

[27] W. Sun, R. Baize, C. Lukashin, and Y. Hu, "Deriving polarization properties of desert-reflected solar spectra with PARASOL data", *Atmos. Chem. Phys.*, Vol. 15, pp. 7725–7734, 2015; doi:10.5194/acp-15-7725-2015.

[28] G. W. Kattawar and G. N. Plass, "Radiance and Polarization of Light Reflected from Optically Thick Clouds", APPL. Opt., Vol. 10, Issue 1, pp. 74-80, 1971.

[29] J. Sun, X. Xiong, E. Waluschka, and M. Wang, "Suomi National Polar-Orbiting Partnership Visible Infrared Imaging Radiometer Suite polarization sensitivity analysis", Appl. Opt., Vol. 55, Issue 27, pp. 7645-7658, 2016; doi: 10.1364/AO.55.007645.